ENGINEERING Energy 2026, 20(2): 10473
https://doi.org/10.1007/s11708-026-1047-3

RESEARCH ARTICLE

A novel design of C_{16}DMAAC-modified solid-state polymer electrolyte reinforcing battery stability and lifetime

Dong Yang[1], Shifeng Zhang[2], Daiman Zhu[1], Xueling Liu[1], Yan Chai[1], Rui Gao (✉)[1], Liang Wang[2], Yongli Li (✉)[1]

1 Institute for Clean Energy Technology, North China Electric Power University, Beijing 102206, China
2 State Grid Shanxi Electric Power Company, Electric Power Research Institute, Taiyuan 030001, China

HIGHLIGHTS

- The novel design grafts C_{16}DMAC onto PMMA to prevent salt aggregation.
- The modified electrolyte achieves a high ionic conductivity and a high Li-ion transfer number.
- This approach promotes a robust SEI layer and suppresses lithium dendrites.
- The full cell exhibits excellent cycling stability and rate capability.

Keywords:
Gel polymer electrolytes (GPEs)
Quaternary ammonium salt
Solid-state battery
Li-ion conductivity
Hexadecyl dimethyl allyl ammonium chloride (C_{16}DMAAC)

ABSTRACT

Solid-state electrolytes are crucial for developing next-generation batteries with enhanced safety and energy density. Among them, the polymethyl methacrylate (PMMA)-based gel polymer electrolytes (GPEs) have emerged as promising materials for high-performance battery systems. However, PMMA-based electrolytes suffer from intrinsically low ionic conductivity. While blending with quaternary ammonium salts offers an effective solution, it often leads to salt deposition during cycling, compromising long-term stability. In this work, a novel GPE is developed by grafting long-chain quaternary ammonium salt (C_{16}DMAAC) onto the PMMA backbone. This molecular design simultaneously regulates polymer chain disorder and immobilizes free anions, enabling a high Li-ion transfer number of 0.59, ionic conductivity of 7.23×10^{-4} S/cm, and an expanded electrochemical stability window of 4.9 V. Moreover, the incorporated ammonium cations in the C_{16}DMAAC segment optimize the Li^+ solvation structure, promoting the formation of a robust, inorganic-rich solid electrolyte interphase (SEI). The excellent cycling stability is demonstrated by the Li||NCM811 full cell, which retains 92% of its initial capacity over 200 cycles at 0.5 C, and 80% retention after 300 cycles at 2 C. This work presents a promising strategy for designing novel electrolyte structures by grafting quaternary ammonium salts into polymer chains to improve battery stability and lifespan.

1 Introduction

Lithium-ion batteries (LIBs) are widely used in energy storage systems, electric vehicles, and 3C electronics. As performance demands continue to rise, especially for higher energy density and improved safety, researchers are increasingly focusing on next-generation battery systems that strike a balance between these requirements [1,2].

Current investigations indicate that major safety concerns stem from the use of flammable organic liquid electrolytes and unstable separators. As a key component of the battery, the electrolyte not only serves as Li^+ transport medium but also physically separates the cathode and anode. Although conventional liquid electrolytes, such as currently widely used carbonate-based electrolytes, offer high ionic conductivity (> 10^{-3} S/cm) and good interfacial compatibility with electrodes, their volatility and flammability pose serious safety risks, thereby limiting their suitability for high-energy-density applications [3].

To reduce dependence on liquid electrolytes and mitigate their associated risks, solid-state electrolytes (SSEs), including inorganic types (e.g. $Li_7La_3Zr_2O_{12}$, $Li_{1+x}Al_xTi_{2-x}(PO_4)_3$, $Li_{10}GeP_2S_{12}$) and organic polymer electrolytes (e.g. polyethylene oxide, polyvinylidene

✉ Corresponding authors. E-mails: r55gao@ncepu.edu.cn (R. Gao); yongli.li@ncepu.edu.cn (Y. Li)

Article history: Received 20 July 2025, Revised 8 September 2025, Accepted 16 October 2025, Available online 1 January 2026

fluoride), have been extensively studied [4–7]. These materials exhibit superior mechanical robustness, effectively help suppress the formation of lithium dendrites, and offer intrinsic safety benefits [8]. However, their widespread application is hindered by drawbacks such as low ionic conductivity and significant interfacial resistance between the rigid electrode and the electrolyte [9].

Relevant studies have revealed that gel polymer electrolytes (GPEs) have emerged as a promising solution by combining the benefits of solid and liquid electrolytes, offering enhanced safety and better electrochemical performance [10,11]. Among various GPEs systems, polymethyl methacrylate (PMMA)-based GPEs stand out due to their excellent film-forming ability and chemical stability [12,13]. Nevertheless, traditional PMMA-based GPEs still suffer from insufficient Li^+ conductivity at room temperature.

Recent investigations have shown that incorporating organic quaternary ammonium salts into GPEs can effectively promote lithium salt dissociation via ion-dipole interactions and significantly suppress anion migration due to their bulky structure, thereby enhancing Li-ion conductivity [14]. For instance, Chai et al. [15] showed that adding tetrabutylammonium iodide (TBAI) to Jatropha oil-based polyurethane acrylate promoted ion dissociation and migration, achieving an ionic conductivity of 1.88×10^{-4} S/cm. Phiri et al. [16] demonstrated that incorporating a large-dipole benzotriazole (BT)-based zwitterionic salt promoted lithium salt dissociation and doubled the ionic conductivity compared to the unmodified sample, while also improving electrochemical stability. Similarly, Zhang et al. [17] reported that quaternary ammonium salt additives provide dual functionality from both cations and anions, enabling high ionic conductivity, enhanced interfacial stability even at −60 °C, improved voltage tolerance, and reduced desolvation energy barriers.

However, these benefits are typically limited when quaternary ammonium salts are used as additives physically blending into electrolyte. Localized salt aggregation and uneven deposition can lead to a non-uniform solid electrolyte interphase (SEI) formation and reduced cycling stability [18].

To address the stability issues induced by quaternary ammonium salt additives while maintaining high Li^+ mobility in GPEs, it is crucial to ensure the uniform distribution of quaternary ammonium salts within the electrolyte. A promising approach is to graft the quaternary ammonium salt onto the polymer chain through copolymerization. This approach not only enhances the disorder of the GPE chains but also ensures even dispersion of the quaternary ammonium salts within the electrolyte, thereby preventing local aggregation and promoting long-term stability. Despite its potential, this approach remains largely underexplored in the context of optimizing PMMA-based GPEs for both high Li-ion conductivity and favorable stability.

In this study, a novel GPE was developed via *in situ* copolymerization. The quaternary ammonium salt hexadecyl dimethyl allyl ammonium chloride (C_{16}DMAAC) was covalently grafted onto the PMMA backbone through carbon–carbon double bonds. This modification increases polymer chain disorder and ensures quaternary ammonium salt uniform distribution throughout the GPE. Compared with traditional blending methods, this copolymerization strategy can better leverage both the structural advantages of the polymer and the electrostatic effects of the quaternary ammonium salt. The resulting GPE demonstrates three outstanding features:

① The incorporation of C_{16}DMAAC increases the disordered degree of polymer, enabling fast Li^+ migration and enhancing the Li-ion conductivity.

② The cationic groups of C_{16}DMAAC coordinate with anions to increase both Li-ion transfer number and conductivity, while the stable copolymerization structure prevents salt deposition, collectively ensuring enhanced interfacial stability.

③ The presence of ammonium cations in C_{16}DMAAC optimizes the solvation configuration of the lithium salt, boosting the formation of aggregates (AGGs), which in turn facilitates the development of a robust inorganic predominant SEI.

As a result, the GPE exhibits a high ionic conductivity of 7.23×10^{-4} S/cm at room temperature, along with an improved Li-ion transference number of 0.59 and an electrochemical stability window up to 4.9 V. Additionally, the assembled Li|GPE|$LiNi_{0.83}Co_{0.11}Mn_{0.06}O_2$ (NCM811) full cells deliver a high capacity retention of 92% after 200 cycles at 0.5 C, and a high capacity retention of 80% and 76% after 300 cycles even at 2 C and 5 C, highlighting its significant potential for fast-charging batteries.

This work introduces an innovative strategy for designing high-performance, intrinsically safe GPEs through quaternary ammonium salt copolymerization, offering valuable insights for the future development of next-generation lithium batteries.

2 Experimental section

2.1 Preparation of GPEs and battery assembly

The GPEs were prepared using methyl methacrylate (MMA) monomer, C_{16}DMAAC monomer, and bisdehydrodoisynolic acid (BDDA) as a crosslinking agent via in situ thermal polymerization. By varying the amount of C_{16}DMAAC, samples were prepared

with C_{16}DMAAC accounting for 0 wt% (mass fraction), 2 wt%, and 5 wt% of the total polymer mass. Each formulation included 80 wt% liquid electrolyte. 2,2'-Azobis(2-methylpropionitrile) (AIBN) was used as the initiator and thermal polymerization was employed to synthesize the GPEs.

The liquid electrolyte used in this work consisted of 1.0 mol/L LiTFSI dissolved in a solvent mixture of ethylene carbonate (EC), diethyl carbonate (DEC), and ethyl methyl carbonate (EMC) in a 1:1:1 vol% (volume fraction).

For coin cell assembling, a Celgard 2500 separator was adopted, and the precursor solution was introduced into CR2025 coin cell. GPEs were placed between two pieces of lithium foil to construct Li||Li symmetric cells. Full cells were assembled using pre-prepared NCM811 and manganese-based Li-rich cathode, with lithium foil as the counter electrode, following the same procedure. The areal loading of cathode materials was controlled at 2.5 mg/cm^2.

All cells underwent *in situ* polymerization at 70 °C for 6 h and were assembled inside an argon-filled glove box, where levels of oxygen and moisture were maintained at less than 0.01 ppm.

Further details of the battery assembling process are provided in Electronic Supplemenatry Material (ESM).

2.2 Structure characterizations of electrolyte

The surface microstructure, elemental distribution, and polymerization degree of the samples were characterized using scanning electron microscope (SEM), energy-dispersive X-ray spectroscopy (EDS), and Fourier-transform infrared spectroscopy (FTIR). Raman spectroscopy (HORIBA LabRAM HR), FTIR, thermogravimetric analysis (TGA), and X-ray photoelectron spectroscopy (XPS) were used to analyze the solvation structure and the composition of the solid electrolyte interphase (SEI) formed on the lithium metal surface after charge-discharg cycling. Nano-computed tomography (Nano-CT) was performed at 4W1A beamline of the Beijing Synchrotron Radiation Facility. Detailed experiment setup procedures are provided in the ESM.

2.3 Electrochemical tests of electrolyte

All electrochemical tests were conducted using coin cells. The ionic conductivity of the GPE and the oxidation voltage under practical conditions were measured using electrochemical impedance spectroscopy (EIS) and floating charge tests, respectively, conducted on a Princeton VersaSTAT4 workstation. The electrochemical stability window of the GPE and the Li-ion transfer number (t_{Li^+}) were determined using a VersaStudio electrochemical workstation. Lithium deposition/stripping experiments were performed using Li||Li symmetric cells. Performance testing of the full cells was conducted through rate capability and long-term cycling tests within a voltage range of 2.5 to 4.3 V. Additional experiment details, including electrochemical test procedures and Li-ion conductivity calculations, are provided in the ESM.

3 Results and discussion

3.1 Synthesis and structure identification of GPEs

The stability issues of traditional physically blended GPEs are mainly reflected in large overpotential, short lifespan, and poor rate capability. To address these challenges, this work proposes a quaternary ammonium salt modification strategy, in which hexadecyl dimethyl allyl ammonium chloride (C_{16}DMAAC) is chemically incorporated into the polymer backbone. A macromolecular cross-linked agent, BDDA, was selected to construct the network of P(MMA-co-C_{16}DMAAC) copolymers via radical polymerization. The long-chain structure of BDDA exhibits better mechanical property compared with small-molecule agents such as ethylene glycol dimethacrylate (EGDMA) [19].

Figure 1(a) shows the monomer molecular structure and crosslinking process of BDDA-P(MMA-co-C_{16}DMAAC). MMA and C_{16}DMAAC monomers were efficiently copolymerized within the function of AIBN as the initiator. The bis-acrylic functional group of BDDA reacts with the free radical sites of the monomer molecular to form a stable crosslinked network. The condition of optimized polymerization was set at 70 °C for 6 h. The resulting precursor mixture solidified completely, showing no flow in an inverted reagent bottle after polymerization, as shown in Fig. 1(a), confirming successful polymerization.

Figure 1(b) presents the FTIR spectra of the GPE, providing molecular-level evidence for the successful formation of BDDA-P(MMA-co-C_{16}DMAAC) and key structural transformations. Characteristic absorption bands at 1180 and 1730 cm^{-1} correspond to the C–O–C and C=O stretching vibrations, respectively, originating from MMA and BDDA. The absorption at 1635 cm^{-1}, attributed to the stretching vibration of C=C bonds in the monomer [20,21], disappears after polymerization, indicating complete conversion of the monomers. During polymerization, the thermal initiator AIBN decomposes at 70 °C to generate two 2-cyanopropyl primary radicals, which subsequently initiate polymerization by attacking the C=C bonds in MMA and C_{16}DMAAC. Simultaneously, the cross-linked agent (BDDA) breaks π bonds and reacts to form monomer free radicals, thereby initiating

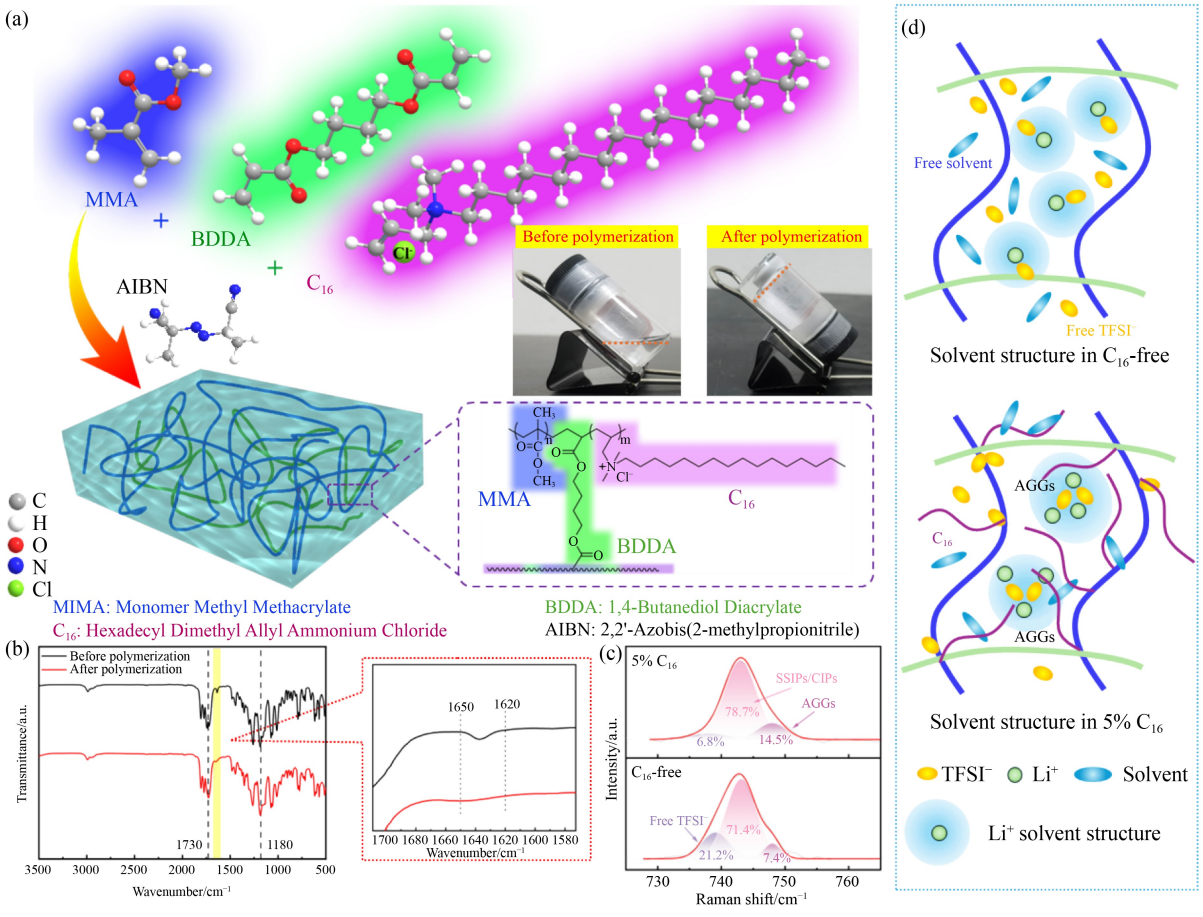

Fig. 1 Preparation of electrolyte and characterizations on *in situ* polymerization.

(a) Polymerization process of MMA, BDDA, and C_{16}DMAAC initiated by AIBN (The insert photos are optical images of the monomer mixture before and after polymerization.); (b) FTIR spectra of monomer mixture before and after polymerization; (c) Raman spectra of GPEs at different C_{16}DMAAC concentrations; (d) schematic diagram of Li^+ solvent structure in GPE with and without C_{16}DMAAC.

chain reactions. Moreover, the free radicals of monomer can attack other C=C bonds continuously and rapidly, and the continuous addition with opening π bonds occurs recurrently, resulting in reactions of chain growth [22]. The detailed process of AIBN participated polymerization is illustrated in Fig. S1.

Finally, the radical polymerization is completed through coupling or disproportionation termination. Compared with traditional PMMA, the network structure formed by MMA, C_{16}DMAAC, and BDDA significantly enhances the mechanical stability of GPE. To further verify this improvement, the method reported by Zhang et al. [19] was adopted, in which GPE films were coated onto lithium metal substrate to evaluate mechanical reinforcement. The mechanical properties of the GPE were investigated by measuring Young's modulus using atomic force microscopy (AFM). The results indicated that the C_{16}-free sample exhibited a modulus of approximately 1.2 GPa, while the sample with 2% C_{16}DMAAC addition showed a more than twofold increase, to approximately 2.8 GPa. Moreover, through copolymerization, quaternary ammonium ions of C_{16}DMAAC can be well inserted into the polymer matrix, avoiding deposition of quaternary ammonium salts and improving electrolyte stability. More importantly, covalent incorporation of quaternary ammonium ions via copolymerization not only prevents deposition but also enables anion coordination, thus collectively improving the Li-ion transference number and overall electrochemical stability.

The solvation structures of Li^+ in GPE were evaluated to forecast the electrochemical performances [23]. Raman spectroscopy was employed to provide insights into the Li^+ solvation shell structures, as illustrated in Fig. 1(c). Peaks at 739, 743, and 748 cm^{-1} correspond to distinct coordination states of $TFSI^-$: free anions, solvent-separated ion pairs (SSIPs), contact ion pairs (CIPs), and aggregates (AGGs) [24]. Compared with the C_{16}-free sample, the 5% C_{16} sample exhibits a significant spectral shift, indicating a higher proportion of SSIPs/CIPs and AGGs. The quaternary ammonium group in C_{16}DMAAC

segment carrying positive charge interacts with $TFSI^-$ anions, suppressing its migration, reducing the number of free $TFSI^-$ anions and facilitating the formation of AGGs. The presence of AGGs reduces dipole interactions with Li^+ and attributes to Li^+ solvation shell structures as shown in Fig. 1(d) [25,26].

Notably, the fraction of AGGs increases from 7.4% in the C_{16}-free system to 14.5% in the 5% C_{16}DMAAC sample, confirming the critical role of C_{16}DMAAC in enhancing Li^+–$TFSI^-$ interactions and promoting the formation of highly coordinated complexes. These findings are further supported by FTIR analysis as shown in Fig. S2. The absorption peak near 740 cm^{-1} corresponds to the S–N–S bending vibration of $TFSI^-$. The addition of C_{16}DMAAC in GPE promotes formation of AGGs in the electrolyte, leading to a noticeable blueshift of this characteristic absorption. A similar trend is observed in TGA analysis (Fig. S3). The more gradual thermal desorption curve indicates that more solvent molecules are fixed onto the polymer framework, thereby elevating the temperature at which the solvent begins to volatilize. A higher concentration of AGGs in the electrolytes contributes to optimized SEI composition and improved lithium deposition behavior in LMBs [27].

Figures 2(a) and 2(b) shows the SEM images of the Celgard 2500 separator and the polymerized electrolyte film, respectively. In this work, Celgard 2500 serves as both the primary separator and an electrolyte holster in a GPE-based battery system, in which liquid will first infiltrates into the pores of Celgard 2500 and is then in-situ polymerized to form the final GPE structure.

Figures 2(b) and S4 compare the surface morphologies of GPEs with and without C_{16}DMAAC. The results reveal that both conventional and modified GPEs exhibit similar surface porosity. These pores are primarily attributed to the high-vacuum environment during SEM imaging, which leads to partial evaporation of the solvent phase in the GPE, thereby revealing the underlying porous structure.

As shown in Fig. 2(c), the cross-sectional SEM image reveals that the GPE maintains a uniform thickness of approximately 25 μm, consistent with the original

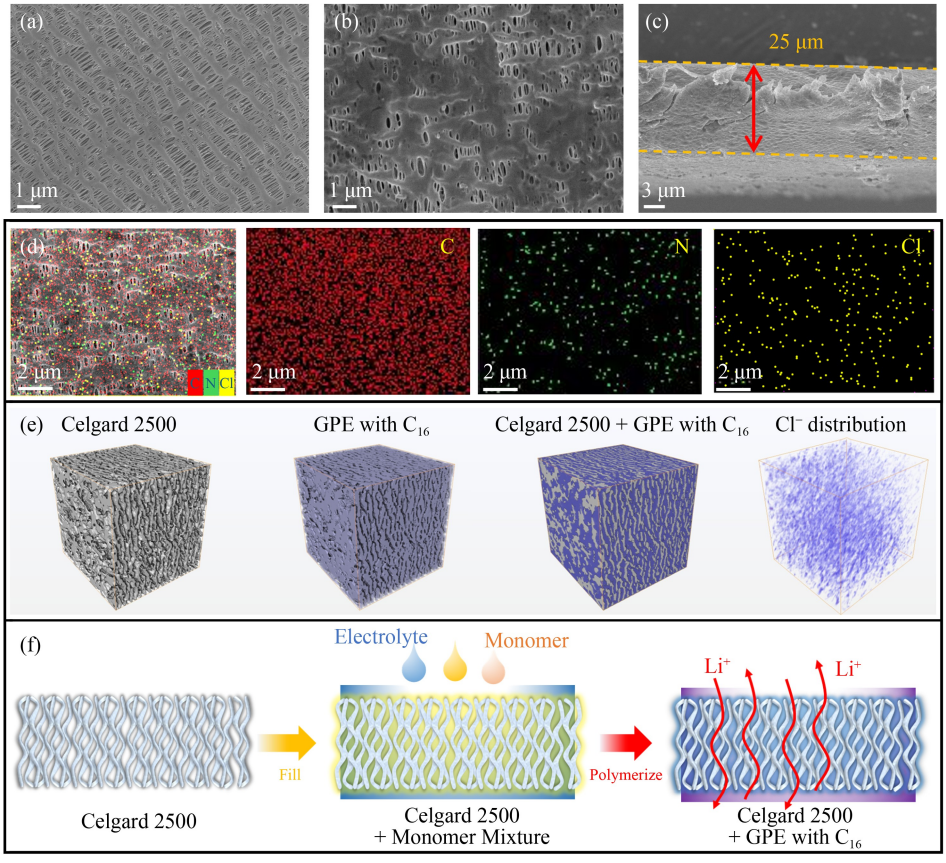

Fig. 2 GPE structure and element division.

(a) SEM image of the Celgard 2500; (b) surface images of the GPE; (c) cross-sectional scanning electron microscopy images of the GPE; (d) SEM image and the corresponding EDS mappings of GPE; (e) reconstruction results of the separator and GPE based on-CT, with a volume size of 25 μm × 25 μm × 25 μm; (f) schematic diagram of *in situ* polymerizes in Celgard 2500.

thickness of the Celgard separator. Meanwhile, EDS elemental mapping of the GPE confirms that nitrogen (N) and chlorine (Cl), derived from the C_{16}DMAAC monomer, are uniformly dispersed across the entire gel electrolyte (Fig. 2(d)). This uniform elemental distribution implies that the copolymerization of MMA and C_{16}DMAAC effectively prevents quaternary ammonium salt agglomeration.

To further assess the GPE infiltration and distribution within the separator, nano-CT was performed at a synchrotron radiation facility using Zernike phase-contrast mode to enhance contrast between the GPE and separator structure. A representative region of the GPE and separator was selected for 3D reconstruction and segmentation, as shown in Fig. 2(e). In the 3D rendering, the white solid phase corresponds to the Celgard separator skeleton, while the purple phase represents the C_{16}DMAAC-containing GPE. The images confirm that the GPE thoroughly infiltrates the pores of the separator, with no significant voids observed in the 3D reconstruction. This result verifies that, under practical polymerization conditions, the pores of separator are indeed completely filled by GPE. The uniformity of GPE distribution provides a structural foundation for the subsequent construction of the lithium-ion transport channels.

To further evaluate the distribution of the grafted C_{16}DMAAC in the GPE, chlorine (Cl) was used as a marker element of C_{16}DMAAC due to its relatively high absorption of X-ray. As shown in the final volume rendering in Fig. 2(e). Cl is uniformly distributed throughout the GPE, with no obvious signs of aggregation or phase separation. This observation supports the conclusion that C_{16}DMAAC was successfully incorporated into the PMMA backbone to form a homogeneous P(MMA-co-C_{16}DMAAC) copolymer, thereby avoiding the C_{16}DMAAC phase aggregation and localized deposition.

Based on the combined results from SEM and nano-CT analyses, the *in situ* polymerization process of uniform formation of the GPE within the Celgard 2500 separator is demonstrated in Fig. 2(f).

3.2 Electrochemical tests and Li^+ plating/stripping behaviors

Lithium-based half-cells and symmetric cells were assembled for subsequent electrochemical measurements. Initially, EIS was used to determine the ionic conductivity of GPEs at various temperatures. The ionic conductivities at 25 °C for the C_{16}-free, 2% C_{16} and 5% C_{16} GPEs samples were calculated to be 5.34×10^{-4} S/cm, 7.23×10^{-4} S/cm and 1.10×10^{-3} S/cm, respectively (Figs. S5(a) and 5(b)). This improvement in ionic conductivity upon C_{16}DMAAC grafting is attributed to the unique cross-linked network structure and the dipole features introduced by C_{16}DMAAC.

To gain deeper insights into the impact of C_{16}DMAAC on ion transport kinetics, temperature-dependent ionic conductivity, measurements were performed as shown in Figs. 3(a) and S5. Activation energies (E_a) values, derived from Arrhenius fits, were 0.21 eV (C_{16}-free), 0.16 eV (2% C_{16}), and 0.13 eV (5% C_{16}). The GPE containing 5% C_{16} exhibits the lowest E_a, indicating that the incorporation of C_{16}DMAAC effectively reduces the ion migration barrier, enhancing ionic mobility conductivity [28].

The electrochemical stability windows of the GPEs were evaluated using linear sweep voltammetry (LSV) in Li||stainless steel cells. As shown in Fig. 3(b), both the 2% C_{16} and 5% C_{16} samples demonstrate an extended oxidation stability limit up to 4.9 V, surpassing the C_{16}-free counterpart. This indicates their strengthened tolerance against electrochemical oxidation and superb congruity with high-voltage lithium metal batteries.

To better understand the benefits of C_{16}DMAAC addition in compatibility with cathodic materials, electrochemical floating test was conducted on Li||$LiNi_{0.83}Co_{0.11}Mn_{0.06}O_2$ (NCM811) cells using different GPEs (Figs. 3(c) and S6). The 2% C_{16} sample showed leakage current increase above 4.9 V, consistent with LSV result, with a significant rise at 5.2 V. In contrast, as the voltage increased from 4.3 V, both the C_{16}-free and 5% C_{16} samples maintained stable currents up to 5.1 V, likely due to the inherent antioxidant nature of the carbonic-ester-based electrolyte. These results indicate that an appropriate amount of C_{16}DMAAC addition can enhance the compatibility and electrochemical stability of high-voltage cathode materials.

The improved electrochemical stability observed in Figs. 3(b) and 3(c) for the C_{16}DMAAC-modified GPE is attributed to the covalent polymerization of quaternary ammonium groups via copolymerization with MMA. This process effectively anchors positively charged quaternary ammonium cations onto the polymer backbone, forming a stable 3D network. The copolymerized structure from C_{16}DMAAC significantly increases the disorder of polymer chain and avoids aggregation and precipitation commonly observed in conventional blended quaternary ammonium salts. Moreover, the positively charged polymer chains with quaternary ammonium cations can coordinate with anions and solvent molecules, reducing free solvent in the GPE and decreasing the likelihood of undesired side reactions [29].

In addition, the Li-ion transfer number (t_{Li^+}) was evaluated based on the potentiostatic polarization curves (Figs. 3(d) and S7). Values of t_{Li^+} increased from 0.25

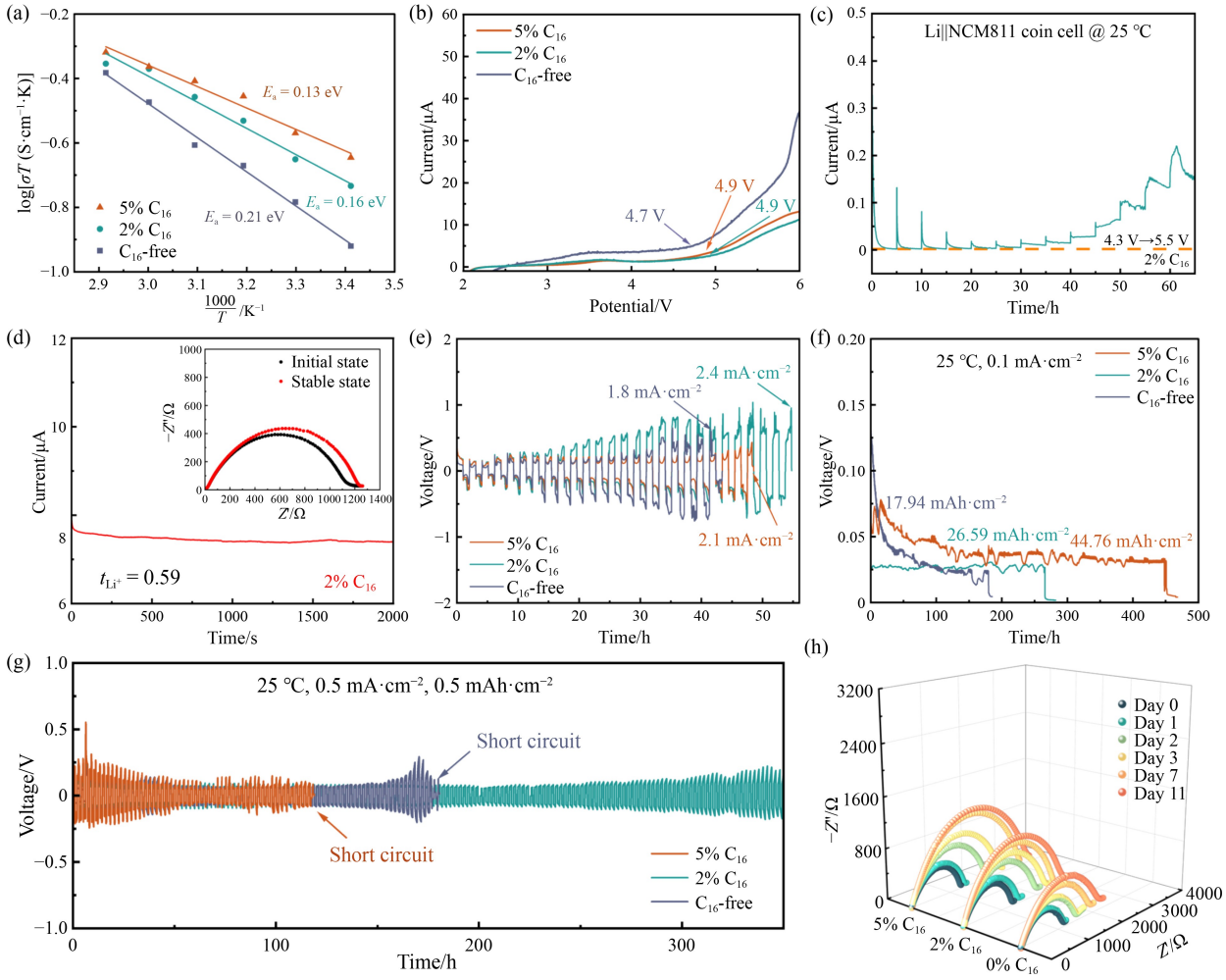

Fig. 3 Electrochemical properties of GPEs.

(a) Ionic conductivity of GPEs at different temperatures (20–70 °C); (b) LSV curves measured at a scan rate of 0.1 mV/s; (c) electrochemical floating test curves of Li||2% C_{16}-GPE||NCM811 ranging from 4.3 to 5.5 V, step 0.1 V; (d) chronoamperometry curve of Li||Li symmetric cell with 2% C_{16}-GPE and EIS Nyquist plots before and after polarization; (e) critical current density measurement of Li||Li symmetric cell with different GPEs under current densities from 0.02 to 2.40 mA/cm^2; (f) galvanostatic long-term discharge curves of different GPEs at a current density of 0.1 mA/cm^2; (g) cycling performance of Li symmetric cells with different GPEs at 0.5 mA/cm^2@ 0.5 mAh/cm^2; (h) time dependent impedance evolutions of Li||Li symmetric cells with different GPEs.

(C_{16}-free) to 0.59 (2% C_{16}) and 0.60 (5% C_{16}), consistent with corresponding EIS data. The increase in t_{Li^+} is attributed to the structural features of C_{16}DMAAC, where the introduction of long-chain and cationic active sites to GPE enables interactions with $TFSI^-$ anions, restricting their migration and reducing dipole interactions with Li^+, thereby promoting Li^+ transport [30]. Based on the space charge model, a greater Li-ion transfer number ($t_{Li^+} > 0.5$) effectively alleviates concentration polarization at the electrode-electrolyte interface, inhibiting lithium dendrite growth, and improving the stability of the lithium anode under high current densities [31].

Figure S8 compares the sample developed in this work and representative results from the literature, showing that the C_{16}-incorporated GPE exhibits superior overall performance, especially in ionic conductivity, Li-ion transfer number, and electrochemical stability window. Benefiting from these combined effects, the GPE with 2% C_{16} demonstrates a critical current density (CCD) of 2.4 mA/cm^2, outperforming both the C_{16}-free (1.8 mA/cm^2) and the 5% C_{16} (2.1 mA/cm^2) samples (Fig. 3(e)).

Galvanostatic polarization curves of Li||Li symmetric cells constructed using different GPEs at a current density of 0.1 mA/cm^2 (Fig. 3(f)) reveal that the cell incorporating 5% C_{16} achieves a notably higher areal capacity utilization of 44.76 mAh/cm^2 compared to 17.94 and 26.59 mAh/cm^2 for the C_{16}-free and 2% C_{16}

cells, respectively. This performance exceeds that of previously documented composite polymer electrolyte based on PAN/PVDF-HFP@HKUST-1, which showed 41 mAh/cm^2 [32]. These results indicate that adding C_{16}DMAAC to the PMMA polymer gel electrolyte significantly enhances the lithium accommodation capability, making it better suited to pair with high-loading cathodes in practical applications.

To further assess the stability associated with lithium metal and the high-rate performance, galvanostatic cycling tests were conducted on lithium symmetric cells at 0.5 mA/cm^2 and the areal capacity of 0.5 mAh/cm^2 (Figs. 3(g) and S9). The 2% C_{16} sample demonstrates remarkably stable lithium stripping/plating with no significant increase in polarization over 350 h, outperforming the C_{16}-free electrolyte. However, unexpectedly, the 5% C_{16} sample exhibited a severe degradation in performance and a short circuit at 118 h, earlier than 178 h observed for the C_{16}-free electrolyte. This decline is attributed to excessive addition of C_{16}DMAAC which increases the side reactions at the interface between the gel electrolyte and lithium anode, leading to the decomposition of the gel electrolyte and causing a short circuit, as suggested by the voltage fluctuations at about 100 h in Fig. 3(g).

In situ EIS was used to monitor the evolution of electrochemical resistance over time in Li||Li symmetric cells to investigate the stability of interface between the GPEs and the lithium anode. As shown in Fig. 3(h), the interfacial impedances of the three gel electrolytes with different concentrations of C_{16}DMAAC are nearly identical in the first two days, while the addition of 5% C_{16} shows a significant impedance increase, reaching its highest over time, further validating the proposed degradation mechanism. To further verify this process, SEM images of the lithium metal surface were obtained after prolonged contact (Fig. S10). In the absence of C_{16}DMAAC, the surface exhibits increased roughness due to corrosive reactions, with some by-products visibly deposited. In contrast, when excessive C_{16}DMAAC is introduced, the surface reactions significantly intensify, leading to an obvious increase in roughness and complete coverage by by-products. This layer of by-products impedes ion transport, consistent with EIS findings.

Moreover, XPS was also used to analyze the surface composition of lithium after the reaction. (Fig. S11) The results clearly indicate that, compared to the 2% addition, excessive C_{16}DMAAC promotes formation of more organic lithium salts on the surface, contributing to increased interfacial impedance. Post-cycling SEM images of cycled lithium symmetric electrodes (Fig. S12) show crack formation on the 5% C_{16} anode surface, indicating poor stability and mechanical integrity of the SEI layer, correlating with the inferior electrochemical performance observed.

In summary, while moderate incorporation of C_{16}DMAAC (2%) significantly enhances ionic conductivity, Li-ion transfer, and cycling stability, excessive addition (5%) induces detrimental side reactions at the lithium interface, compromising long-term performance.

3.3 Full-cell performance with NCM811

Specific electrochemical measures were conducted to evaluate full-cell performance. Li||NCM811 LMBs incorporating C_{16}-free, 2% C_{16}, and 5% C_{16} electrolytes were fabricated, and their rate capabilities and long-term cycling performances were evaluated within a voltage window of 2.7–4.3 V at 25 °C.

Notably, the cell with 2% C_{16} electrolyte exhibited the best rate performance, delivering specific capacities of 192.7, 185.7, 177.7, 157.3, 145.6, and 119.1 mAh/g at 0.1, 0.2, 0.5, 1, 2, and 5 C (where 1 C = 200 mA/g), respectively, as depicted in Fig. 4(a). In contrast, the C_{16}-free electrolyte exhibited slightly lower capacities of 191.8, 184.3, 169.5, 157.2, 143.4, and 100.0 mAh/g at identical rates. In 2% C_{16} system, when the current density was returned to 0.1 C after high-rate cycling, the capacity was restored to 191.9 mAh/g, indicating excellent reversibility and adaptability under different application conditions. Conversely, the C_{16}-free and 5% C_{16} electrolyte demonstrated significantly inferior rate capabilities, with the 5% C_{16} sample failing to maintain 100 mAh/g at 5 C. These observations align with earlier conclusion, where the introduction and covalent confinement of C_{16}DMAAC within the PMMA matrix increased the stability of electrolyte, and the macromolecule BDDA further affects the cross-linked structure enabling excellent electrochemical activity. However, due to side reaction between GPE and lithium metal anode, excessive C_{16}DMAAC (>2%) adversely affects the SEI, as previously discussed.

Figure 4(b) displays the detailed charge/discharge profiles at different current densities. The data reveals that C_{16}DMAAC effectively suppresses overpotential by modulating Li^+ transport kinetics, confirming that the rationally tailored polymer electrolyte facilitates rapid and efficient charge-discharge processes.

Figure 4(c) compares the cycling performance of Li||NCM811 cells with different GPEs at 0.5 C. The 2% C_{16} GPE demonstrated superior cycling stability, retaining 92% of its initial capacity after 200 cycles, corresponding to an average capacity retention of 99.955% per cycle from an initial capacity of 172.2 mAh/g. This is significantly better than the 73% retention for the C_{16}-free electrolyte and 85% for the 5% C_{16} variant. More-

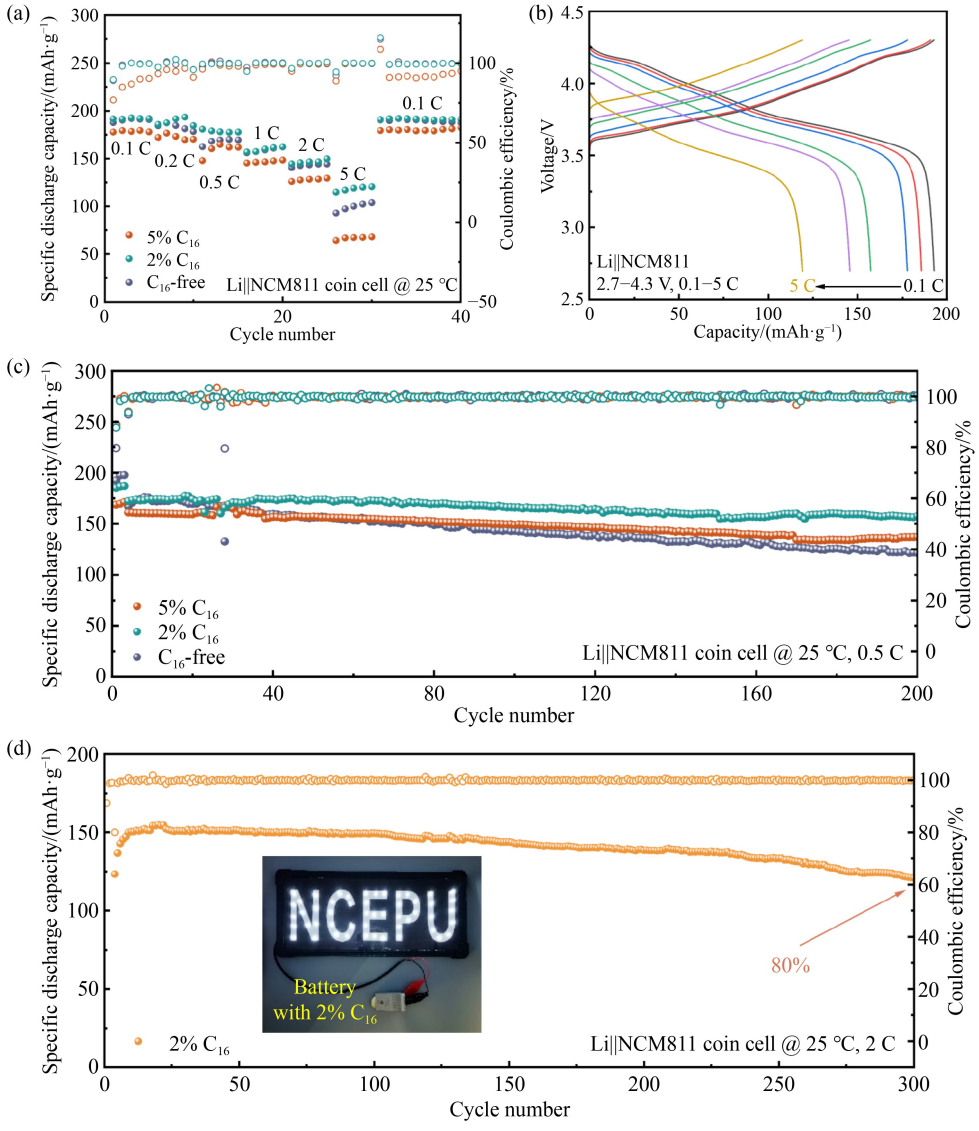

Fig. 4 Electrochemical properties of LMBs at room temperature.

(a) Rate capability of Li||NCM811 coin cells with different GPEs; (b) rate capability charge/discharge curves of Li||NCM811 coin cells with 2% C_{16}-GPE; (c) cycling performance of Li||NCM811 coin cells with different GPEs at 0.5 C; (d) cycling performance of Li||NCM811 coin cells with different GPEs at 2 C (The insert image is the practical application of Li||NCM811 coin cells with 2% C_{16}-GPE to power an LED light.).

over, Fig. S13, shows minimal overpotential increase after 200 cycles, indicating an enhanced Li^+ transport kinetics. These results confirm that C_{16}DMAAC incorporation not only reinforces the polymer network, but also optimizes Li^+ solvation and transfer at the electrolyte/anode interface. The concentration of C_{16} can be adjusted to mitigate side reactions between the GPEs and the lithium metal anode. The results confirm that a 2% addition effectively balances interfacial stability and electrochemical activity, and the corresponding GPE exhibits promising practical potential.

Further tests at high rates and voltages were performed to further evaluate the electrochemical performance of the 2% C_{16} electrolyte. Rate performance tests on Li||NCM811 full cells at 2 and 5 C (Figs. 4(d) and S14) demonstrated excellent cycling stability, with capacity retentions exceeding 80% and 76% after 300 cycles, respectively, providing solid evidence for high Li^+ transfer and stable structure.

Moreover, to verify the compatibility of the electrolyte with higher voltage, lithium-rich manganese-based (LMNCO) cathode was tested at elevated cutoff voltages of 4.6 and 4.9 V, as shown in Fig. S15. The full cells with 2% C_{16}-containing electrolyte maintain stable

performance under these conditions, validating the role of C_{16}DMAAC in expanding the electrochemical stability window and enabling use in high energy density systems.

To evaluate the practical applicability of the as-prepared C_{16} GPEs, full cells with NCM811 cathode were assembled and successfully used to power an LED light (Fig. 4(d) insert image). This highlights the potential of the C_{16}DMAAC-grafted GPE to replace conventional liquid electrolyte in advanced lithium metal batteries.

In summary, these results confirmed that the novel C_{16}DMAAC-modified PMMA-based GPE offers excellent electrochemical performance combining high ionic conductivity, interfacial stability, and wide electrochemical window, making it a promising electrolyte for next-generation high-energy lithium metal batteries.

3.4 Interface reaction mechanism of Li/GPE

From the above electrochemistry performance, it can be concluded that C_{16}DMAAC-modified GPE exhibits high stability, excellent voltage tolerance, and superior Li-ion conductivity. To further investigate the interface reaction mechanism between Li and GPE, in situ EIS measurements were conducted at various charge and discharge states.

As shown in Fig. S16, the interfacial charge-transfer resistance after initial cycling is lower than that in the pristine state. This reduction can be attributed to the gradual formation and stabilization of the SEI film, which fully activates of the electrode-electrolyte interface. In contrast, the battery without C_{16}DMAAC exhibits the highest initial resistance (approximately 600 Ω). Although the charge-transfer resistance (R_{ct}) decreases significantly over successive cycles, this reflects unstable interfacial kinetics in the unmodified system.

Conversely, the incorporation of C_{16}DMAAC helps maintain relatively stable interfacial kinetics. This may be due to the ability of the quaternary ammonium cation to modulate the Li^+ solvation structure and stabilize the electrochemical interface. However, a higher C_{16}DMAAC content leads to an increased final R_{ct}. Notably, the battery with 5% C_{16}DMAAC shows more than twice the resistance of the 2% C_{16} sample, suggesting that excessive C_{16}DMAAC tends to react more readily with lithium metal, forming an interfacial layer with lower electrochemical activity that ultimately impairs cell performance. These findings are consistent with the electrochemical results shown in Figs. 3(g) and 3(h).

To evaluate structure changes in different anodes, cycled electrodes were disassembled and analyzed morphologically and compositionally. SEM and XPS were employed to examine surface and chemical evolution. Figures 5(a)–5(c) displays the surface morphologies of Li anodes paired with C_{16}-free, 5% C_{16}, and 2% C_{16} GPEs after 200 cycles at 0.5 C, respectively.

In Fig. 5(a), the lithium metal surface in the NCM811/C_{16}-free/Li cell appears rough with multiple protrusions, indicating uneven lithium deposition and dendrite growth. In contrast, the anode with 5% C_{16} GPEs (Fig. 5(b)) exhibits only minor surface irregularities, confirming that C_{16}DMAAC effectively inhibits lithium dendrite formation, which aligns with the previous inference. This inhabitation for lithium dendrite is also attributed to enhanced Li^+ migration between GPE and Li anode.

Based on prior conclusion indicating that > 2% C_{16}DMAAC may increase side reaction at the anode, the battery with 2% C_{16} GPE was also examined (Fig. 5(c)). Notably, it shows a smooth and uniform surface, suggesting that 2% C_{16}DMAAC provides optimal dendrite suppression interfacial stabilization.

Figure S17 exhibits the carbon element distribution on a broader scale. In the EDS mapping, the presence of carbon is considered to be associated with organic compounds. A higher and more heterogeneous distribution of carbon suggests a greater presence of organic lithium salts, which is detrimental to anode stability [33]. Compared to the 2% C_{16}-modified sample, the sample without C_{16}DMAAC exhibits a higher carbon signal, further supporting the improved stability of the C_{16}DMAAC-modified electrolyte.

Further composition analysis was conducted through XPS, including etching-assisted depth profiling. XPS is widely used for analyzing surface composition, and argon-ion etching allows detection of subsurface layers. In this work, signal from Cl was first examined on the surface and inner the anode to assess the influence of anions in C_{16}DMAAC. As shown in Fig. S18, no signal from Cl^- was detected on the surface or in the bulk, indicating that chloride ions do not significantly affect the anode.

Figures 5(d) and 5(e) provide XPS patterns and the peak fitting result in the region of C, F, O. The C 1s spectra shown in Figs. 5(d), 5(e) and S19 reveal typical chemical species such as C–C/C–H (284.8 eV) [34], C–O (286.5 eV) [35], C=O (288.6 eV) [36], and CO_3^{2-} (290 eV) [37] across the three electrolytes with varying C_{16}DMAAC concentrations.

Compared to C_{16}-free and 5% C_{16}, the C–C/C–H signal in the 2% C_{16} sample significantly decreases with increasing etching depth, while Li_2CO_3 remains dominant. This indicates that the inner SEI layer in 2% C_{16} primarily consists of inorganic components, which are beneficial for stabilizing lithium metal [38,39].

Previous findings suggest that the positively charged

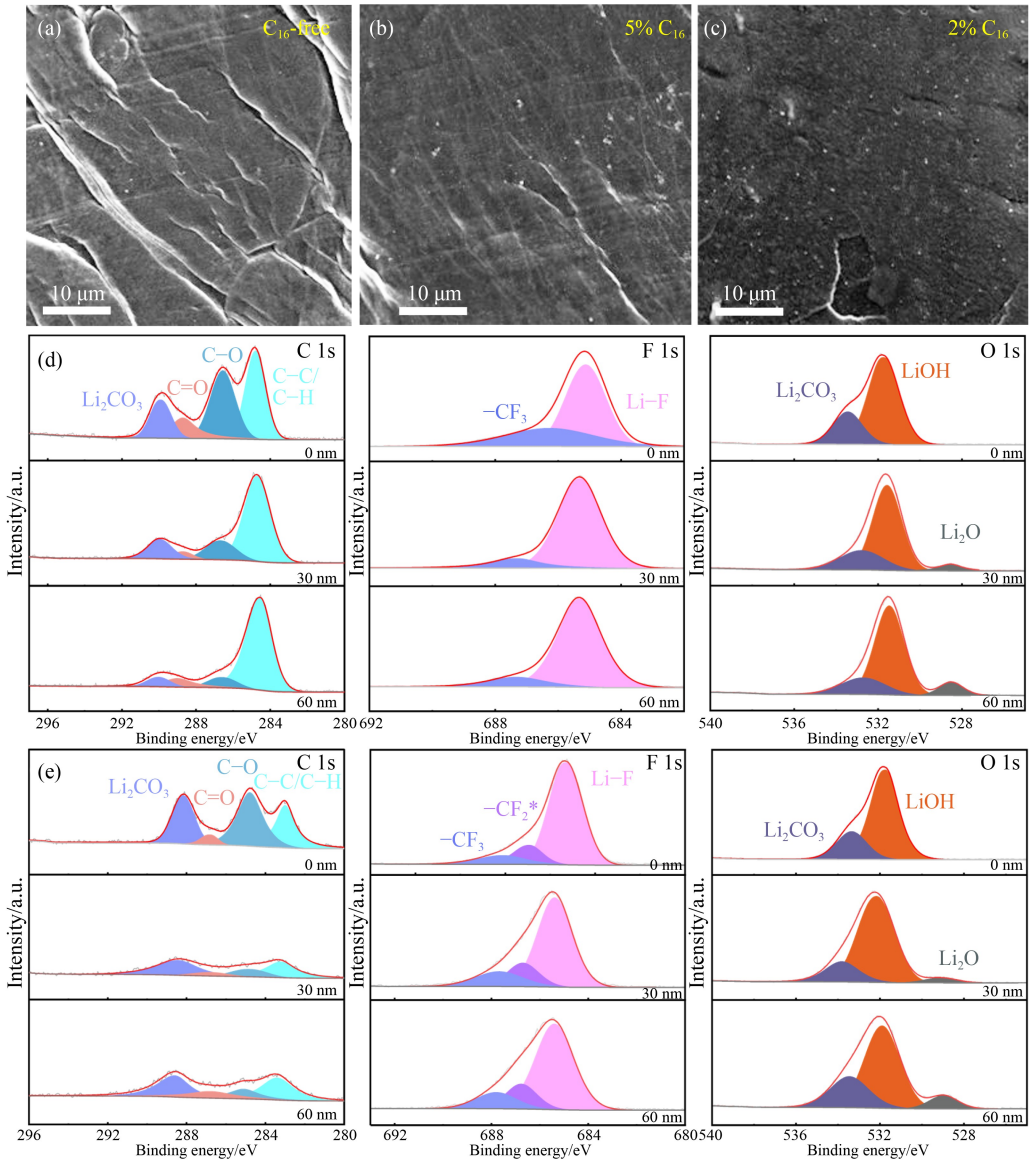

Fig. 5 Chemical composition analysis of cycled Li metal electrodes.

(a) Surface morphologies of Li anodes retrieved from cycled NCM811//Li cells without C_{16}DMAAC additive in the electrolyte (C_{16}-free-GPE); (b) surface morphologies of Li anodes retrieved from cycled NCM811//Li cells with 5% C_{16}DMAAC in the GPE (5% C_{16}-GPE); (c) surface morphologies of Li anodes retrieved from cycled NCM811//Li cells with 2% C_{16}DMAAC in the GPE (2% C_{16}-GPE); (d) XPS depth profiles of C 1s, F 1s, and O 1s for Li electrodes cycled in NCM811//Li cells using C_{16}-free-GPE; (e) XPS depth profiles of C 1s, F 1s, and O 1s for Li electrodes cycled in NCM811//Li cells using 2% C_{16}-GPE.

polymer chains of C_{16}DMAAC coordinate with $TFSI^-$ and solvent molecules, thereby reducing free solvent in content in the GPE. This coordination helps minimize side reactions between free solvent and highly reactive electrodes, effectively suppressing the oxidation of electrolyte. Additionally, the high concentration of AGGs promotes the formation of a favorable SEI composition.

In contrast, the SEI inner layers of the C_{16}-free and 5% C_{16} exhibit higher C–C/C–H content, demonstrating that organic compounds constitute most of the SEI. The high-resolution F 1s spectra reveal Li–F signals (685.2 eV) in all samples [40]. A distinct CF_2 peak at 687.5 eV is observed in the F spectra of both the 2% C_{16} and 5% C_{16} samples due to $TFSI^-$ decomposition, and the CF_2 peak in the 5% C_{16} sample is more pronounced than that in the 2% C_{16} sample, reflecting severe side reactions in the former, consistent with previous conclusions [41–43].

These results confirm that the presence of C_{16}DMAAC segment improve the selectivity of the SEI component by regulating the solvent structure of Li^+, especially favoring

the formation of inorganic component. This contributes to a stable anode environment and supports long cycle life of lithium metal batteries [44].

4 Conclusions

In this work, a novel solid-state electrolyte was developed that demonstrated significantly enhanced ionic conductivity along with improved stability. The new gel GPE was designed by grafting long-chain quaternary ammonium salt (C_{16}DMAAC) into a PMMA-based electrolyte through an in-situ copolymerization strategy. The macromolecular cross-linked agent BDDA was selected to construct the network of P(MMA-co-C_{16}DMAAC) copolymers by radical polymerization.

In contrast to conventional blended electrolyte systems, this molecular design effectively suppresses the issue of quaternary ammonium salt deposition on the anode during cycling, as C_{16}DMAAC is chemically anchored to the PMMA backbone. The grafted C_{16}DMAAC segments not only enhance polymer chain disorder but also promote coordination with $TFSI^-$ anions, thereby increasing the Li-ion transfer number and significantly improving Li-ion conductivity.

It was further demonstrated that the uniform distribution of C_{16}DMAAC within the GPE optimizes the Li^+ solvation structure, facilitating the formation of a robust SEI layer on the anode. With an optimized C_{16}DMAAC content of 2 wt%, the electrolyte achieves a high Li-ion transfer number and a remarkable ionic conductivity of 7.23×10^{-4} S/cm. The electrolyte also exhibits a broad electrochemical stability window up to 4.9 V.

Lithium symmetric cells incorporating this electrolyte demonstrate stable operation for over 300 h without short-circuiting. Full cells employing NCM811 and LMNCO cathodes show excellent cycling stability and high-voltage tolerance. Specifically, the cells retain 92% of their initial capacity after 200 cycles at 0.5 C, and after 300 cycles at high rates of 2 and 5 C, the capacity can still reach over 80% and 76%, respectively.

Overall, this work presents a strategy for constructing high-performance GPE by grafting quaternary ammonium salts onto polymer backbones via in situ thermal polymerization. The resulting electrolyte exhibits significantly enhanced ionic conductivity and high-voltage tolerance, offering a promising pathway toward the design of highly stable, high-energy-density, and safe solid-state battery systems.

Acknowledgements This work was financially supported by the Science and Technology Project of State Grid Shanxi Electric Power Company (No. 520530240022). The contribution of Mr. Xiaodan Bai on materials selection and electrochemical analyzing is greatly acknowledged. Special thanks also go to the 4W1A Beamline of Beijing Synchrotron Radiation Facility (31109.02.BSRF.4W1A) for providing technical support and assistance in nano-CT data collection.

Competing Interests The authors declare that they have no competing interest.

Electronic Supplementary Material Supplementary material is available in the online version of this article at https://doi.org/10.1007/s11708-026-1047-3 and is accessible for authorized users.

References

1. Agnihotri T, Ahmed S A, Tamilarasan E B, et al. Transitioning towards asymmetric gel polymer electrolytes for lithium batteries: progress and prospects. Advanced Functional Materials, 2024, 34(13): 2311215
2. Mennel J A, Chidambaram D. A review on the development of electrolytes for lithium-based batteries for low temperature applications. Frontiers in Energy, 2023, 17(1): 43–71
3. Huang Y, Li J. Key Challenges for grid-scale lithium-ion battery energy storage. Advanced Energy Materials, 2022, 12(48): 2202197
4. Wang X L, Li Y, Liu J, et al. A robust dual-layered solid electrolyte interphase enabled by cation specific adsorption-induced built-in electrostatic field for long-cycling solid-state lithium metal batteries. Angewandte Chemie International Edition, 2025, 64(10): e202421101
5. Lv T T, Liu J, He L J, et al. An ultrathin and robust single-ion conducting interfacial layer for dendrite-free lithium metal batteries. Journal of Energy Chemistry, 2024, 98: 414–421
6. Liao Y L, Wang X L, Yuan H, et al. Ultrafast Li-rich transport in composite solid-state electrolytes. Advanced Materials, 2025, 37(10): 2419782
7. Kundu S, Ein-Eli Y. A review on design considerations in polymer and polymer composite solid-state electrolytes for solid Li batteries. Journal of Power Sources, 2023, 553: 232267
8. Liu F, Gao L, Zhang Z, et al. Interfacial challenges, processing strategies, and composite applications for high voltage all-solid-state lithium batteries based on halide and sulfide solid-state electrolytes. Energy Storage Materials, 2024, 64: 103072
9. Hu L, Gao X, Wang H, et al. Progress of polymer electrolytes worked in solid-state lithium batteries for wide-temperature application. Small, 2024, 20(31): 2312251
10. Zhou Q, He M, Gao S, et al. Molecular regulation and intermolecular chemistry in gel polymer electrolytes for high-voltage lithium batteries. Advanced Science, 2025, 12(18): 2417169
11. Smaran K S, Badam R, Vedarajan R, et al. Flame-retardant properties of in situ sol-gel synthesized inorganic borosilicate/silicate polymer scaffold matrix comprising ionic liquid. Frontiers in Energy, 2019, 13(1): 163–171
12. Long L, Wang S, Xiao M, et al. Polymer electrolytes for lithium polymer batteries. Journal of Materials Chemistry. A, Materials

for Energy and Sustainability, 2016, 4(26): 10038–10069
13. Zhao H, Liu X, Chi Z, et al. Designing a new-type PMMA based gel polymer electrolyte incorporating ionic liquid for lithium oxygen batteries with Ru-based Binder-free cathode. Applied Surface Science, 2021, 565: 150612
14. Liu Y, Qiao S, Hu J, et al. Self-conductive organic quaternary ammonium lithium salt-based ultra-concentrated electrolyte for safe lithium metal batteries. Chemical Engineering Journal, 2024, 496: 154166
15. Chai K L, Aung M M, Noor I M, et al. Observation of ionic conductivity on PUA-TBAI-I_2 gel polymer electrolyte. Scientific Reports, 2022, 12(1): 124
16. Phiri I, Bon C Y, Kim S, et al. Effects of novel benzotriazole based zwitterionic salt as electrolyte additive for lithium ion batteries. Current Applied Physics, 2020, 20(1): 122–131
17. Zhang W, Lu Y, Feng Q, et al. Multifunctional electrolyte additive for high power lithium metal batteries at ultra-low temperatures. Nature Communications, 2025, 16(1): 3344
18. Guo Z, Song X, Zhang Q, et al. Cationic size effect promoting dissolution of nitrate anion in ester electrolyte for lithium–metal batteries. ACS Energy Letters, 2022, 7(2): 569–576
19. Zhang L, Bai M, Wang X, et al. A strong nucleophilic fluorination agent to achieve highly stable *in situ* 3D cross-linked gel polymer electrolyte for lithium-ion batteries. Chemical Engineering Journal, 2024, 481: 148579
20. Zhang X, Zhao S, Fan W, et al. Long cycling, thermal stable, dendrites free gel polymer electrolyte for flexible lithium metal batteries. Electrochimica Acta, 2019, 301: 304–311
21. Jamalpour S, Ghahramani M, Ghaffarian S R, et al. Improved performance of lithium ion battery by the incorporation of novel synthesized organic-inorganic hybrid nanoparticles SiO_2-poly(methyl methacrylate-co-ureidopyrimidinone) in gel polymer electrolyte based on poly (vinylidene fluoride). Polymer, 2021, 228: 123924
22. Li H, Feng T, Gao J, et al. *In situ* construction of 3D crossing-linked gel polymer electrolyte toward high performance and safety lithium metal batteries. Journal of Power Sources, 2024, 618: 235189
23. Wang R, Wu Y, Niu Y, et al. Efficient chemical prelithiation with modificatory Li^+ solvation structure enabling spatially homogeneous SEI toward high performance SiO_x anode. Chinese Journal of Chemistry, 2024, 42(17): 2056–2065
24. Yao S, Guo C, Yang Y, et al. Rigid additives enabling inorganic-rich interphase via steric effects and van der Waals force for stable lithium metal batteries. Advanced Functional Materials, 2025, 35(16): 2419656
25. Zhang J W, Sun J L, Zhao D N, et al. Tuning solvation structure to enhance low temperature kinetics of lithium-ion batteries. Energy Storage Materials, 2024, 72: 103698
26. Qian S, Tan X, Zhu Y, et al. Additives capable of stably supplying anions/cations for homogeneous lithium deposition/stripping. ACS Nano, 2024, 18(50): 34363–34374
27. Weeks J A, Burrow J N, Diao J, et al. *In situ* engineering of inorganic-rich dolid electrolyte interphases via anion choice enables stable, lithium anodes. Advanced Materials, 2024, 36(9): 2305645
28. Jun K, Chen Y, Wei G, et al. Diffusion mechanisms of fast lithium-ion conductors. Nature Reviews. Materials, 2024, 9(12): 887–905
29. Duan S, Zhang L, Zheng Y, et al. "Rigid exterior, soft interior" design enables high-voltage polyether electrolytes for quasi-solid-state batteries. Angewandte Chemie International Edition, 2025, 64(32): e202502728
30. Lin Q, Kundu D, Skyllas-Kazacos M, et al. Perspective on Lewis acid-base interactions in emerging batteries. Advanced Materials, 2024, 36(42): 2406151
31. Zhu J, Zhang Z, Zhao S, et al. Single-ion conducting polymer electrolytes for solid-state lithium-metal batteries: Design, performance, and challenges. Advanced Energy Materials, 2021, 11(14): 2003836
32. Chai Y, Ning D, Zhou D, et al. Construction of flexible asymmetric composite polymer electrolytes for high-voltage lithium metal batteries with superior performance. Nano Energy, 2024, 130: 110160
33. Park C, Kim Y, Lim W G, et al. Toward maximum energy density enabled by anode-free lithium metal batteries: Recent progress and perspective. Exploration, 2023, 4(2): 20210255
34. Ge X, Wu X, Shi Q, et al. Influence of electrical stimulation on the friction performance of $LiPF_6$-based ionic liquids. Lubricants, 2024, 12(5): 167
35. Tu H, Zhang Y, Wu J, et al. Revealing electrochemical process of functional carbon dots stabilized sodium metal anode: Co-deposition and strengthened SEI films. Advanced Functional Materials, 2025, 35(3): 2413488
36. Li X, Liu J, He J, et al. Hexafluoroisopropyl Trifluoromethanesulfonate-driven easily Li^+ desolvated electrolyte to afford Li||NCM811 cells with efficient anode/cathode electrolyte interphases. Advanced Functional Materials, 2021, 31(37): 2104395
37. Zhang J, Wang C, Fu J, et al. Reducing surface roughness to achieve Li_2CO_3-existent lithiophilic interface in garnet-type solid-state batteries. Advanced Functional Materials, 2025, 35(9): 2416229
38. Lim H, Jun S, Song Y B, et al. Rationally designed conversion-type lithium metal protective layer for all-solid-state lithium metal batteries. Advanced Energy Materials, 2024, 14(12): 2303762
39. Wang L, Xu S, Wang Z, et al. A nano fiber–gel composite electrolyte with high Li^+ transference number for application in quasi-solid batteries. eScience, 2023, 3(2): 100090
40. Ren Q, Wang Q, Su L, et al. Inorganic/organic composite fluorinated interphase layers for stabilizing ether-based electrolyte in high-voltage lithium metal batteries. Journal of Materials Chemistry. A, Materials for Energy and Sustainability, 2024, 12(2): 1072–1080
41. Ding F, Li Y, Zhang G, et al. High-safety electrolytes with an anion-rich solvation sructure tuned by difluorinated cations for high-voltage lithium metal batteries. Advanced Materials, 2024, 36(23): 2400177

42. Sun L, Wang Y, Kong L, et al. Designing mesostructured iron (II) fluorides with a stable *in situ* polymer electrolyte interface for high-energy-density lithium-ion batteries. eScience., 2024, 4(1): 100188
43. He Y, Wang L, Wang A, et al. Insight into uniform filming of LiF-rich interphase via synergistic adsorption for high-performance lithium metal anode. Exploration, 2024, 4(2): 20230114
44. Zheng Y, Yang N, Duan S, et al. Dual-enhanced charge transfer through prelithiation strategy in polymer electrolyte enables robust LiF-rich SEI for ultralong-life all-solid-state batteries. Advanced Functional Materials, 2025, e11011